



### Science Arts & Métiers (SAM)

is an open access repository that collects the work of Arts et Métiers Institute of Technology researchers and makes it freely available over the web where possible.

This is an author-deposited version published in: <https://sam.ensam.eu>  
Handle ID: <http://hdl.handle.net/10985/25821>



This document is available under CC BY license

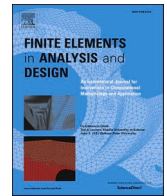
#### To cite this version :

David URIBE, Camille DURAND, Cyrille BAUDOUIN, Regis BIGOT - Enhancing data representation in forging processes: Investigating discretization and R-adaptivity strategies with Proper Orthogonal Decomposition reduction - Finite Elements in Analysis and Design - Vol. 242, p.104276 - 2024

Any correspondence concerning this service should be sent to the repository

Administrator : [scienceouverte@ensam.eu](mailto:scienceouverte@ensam.eu)





# Enhancing data representation in forging processes: Investigating discretization and R-adaptivity strategies with Proper Orthogonal Decomposition reduction

David Uribe<sup>\*</sup>, Camille Durand, Cyrille Baudouin, Régis Bigot

HESAM Université, Arts et Métiers Institute of Technology, Université de Lorraine, LCFC, F-57070, Metz, France

## ARTICLE INFO

### Keywords:

Forging processes  
Proper orthogonal decomposition  
r-Adaptivity  
Adaptative mesh  
Thermomechanical field  
Numerical simulation

## ABSTRACT

Effective data reduction techniques are crucial for enhancing computational efficiency in complex industrial processes such as forging. In this study, we investigate various discretization and mesh adaptivity strategies using Proper Orthogonal Decomposition (POD) to optimize data reduction fidelity in forging simulations. We focus particularly on r-adaptivity techniques, which ensure a consistent number of elements throughout the field representation, filling a gap in existing research that predominantly concentrates on h-adaptivity. Our investigation compares isotropic mesh approaches with anisotropic mesh adaptations, including gradient-based, isolines-based, and spring-energy-based methods. Through numerical simulations and analysis, we demonstrate that these anisotropic techniques provide superior fidelity in representing deformation fields compared to isotropic meshes. These improvements are achieved while maintaining a similar level of model reduction efficiency. This enhancement in representation leads to improved data reduction quality, forming the foundation for data-driven models. This research contributes to advancing the understanding of mesh adaptivity approaches and their potential applications in data-driven modeling across various industrial domains.

## 1. Introduction

Forging processes are often analyzed and optimized using numerical simulations, providing valuable insights into the complex physics involved. While these simulations provide accurate results, their lack of real-time responsiveness limits their applicability in predicting immediate outcomes during forging [1]. Researchers have turned to simulation-based surrogate models to overcome this challenge, leveraging data-driven approaches for real-time predictions [2–4]. Surrogate models offer a promising alternative, connecting input variables to outputs with reduced computational demands compared to traditional simulations [5,6].

However, the data involved in surrogate models often require a reduced representation, as these models typically perform better with scalar data rather than with multi-dimensional data like fields, curves, or complex geometries [7]. This data reduction is commonly achieved through Reduced Order Models (ROMs) [8]. ROMs effectively reduce the dataset's dimensionality from higher to lower dimension. By preserving the essential dynamics of the system, ROMs strike a balance between reduction and performance, facilitating efficient predictions while preserving key characteristics. The original problem is reduced, and the solution is represented

<sup>\*</sup> Corresponding author.

E-mail addresses: [david.santiago.uribe\\_espitia@ensam.eu](mailto:david.santiago.uribe_espitia@ensam.eu) (D. Uribe), [camille.durand@ensam.eu](mailto:camille.durand@ensam.eu) (C. Durand), [cyrille.baudouin@ensam.eu](mailto:cyrille.baudouin@ensam.eu) (C. Baudouin), [regis.bigot@ensam.eu](mailto:regis.bigot@ensam.eu) (R. Bigot).

<https://doi.org/10.1016/j.finel.2024.104276>

Received 6 June 2024; Received in revised form 24 September 2024; Accepted 3 November 2024

Available online 7 November 2024

0168-874X/© 2024 The Authors. Published by Elsevier B.V. This is an open access article under the CC BY license (<http://creativecommons.org/licenses/by/4.0/>).

with far fewer variables, aiming to ensure an accurate solution.

In the manufacturing field, various ROM techniques are employed, including Proper Generalized Decomposition (PGD), Proper Orthogonal Decomposition (POD), the Reduced Basis (RB) method, Dynamic Mode Decomposition, and Hyperreduction techniques [9–11]. Each technique has its own advantages and limitations, and the choice of ROM technique depends on the specific application requirements and the nature of the data involved.

POD is often chosen for its non-intrusive nature [12], as well as its balance of computational efficiency and accuracy [13,14] in data reduction for various applications such as flow modeling [15], laser welding [16], drop oscillations [17], bending [18], sheet metal forming [19,20], composite forming [21], and forging processes [22,23]. However, POD has some potential drawbacks. It often requires a large amount of initial data to capture system dynamics accurately, which can be problematic when data collection is expensive or time-consuming. Additionally, its performance is highly dependent on the system's linearity, and in cases of strong non-linearity, POD may be less effective compared to methods like PGD. Nevertheless, in this study, POD is particularly advantageous, as it will be applied to datasets with varying degrees of non-linearity, allowing for the evaluation of data quality and data reduction performance across different contexts.

In the oversight and quality control of forging parts, monitoring multidimensional thermomechanical fields is common practice. These fields encompass local variables such as deformation, strain rate, temperature, and stress, and are commonly obtained from Finite Element (FE) numerical simulations. In the context of forging processes, these simulations employ a remeshing process to handle large deformations. Remeshing is necessary to preserve the structural integrity of the mesh and to refine it. Consequently, the number of elements and their spatial positions vary at different time steps within the same simulation. As a result, the thermomechanical fields reside in different FE spaces, posing a significant challenge for consistent data representation and reduction.

To address this issue, a common approach is to convert the scattered representation into a uniform mesh of consistent size, effectively discretizing the geometry. This consistent representation of the data across the entire domain should facilitate more reliable data processing and analysis. However, special care must be taken in the uniform mesh generation, as it can significantly impact the representation of the underlying physics [24], and subsequently, the quality of the data reduction.

Various techniques, such as spatial adaptivity [25], discretization and interpolation methods [26], facilitate the generation of uniform meshes. Spatial adaptivity involves dynamically adjusting the mesh to align snapshots within a common finite element space, while discretization and interpolation techniques map data onto a fixed grid. Compared to spatial adaptivity, which requires complex mesh optimization processes, discretization and interpolation methods offer a simpler and more computationally efficient alternative [27,28].

In discretization methods, two major families can be identified. The first is geometry-based discretization, which relies solely on the geometry of the piece, and the second is adaptive discretization, which considers both geometry and the mapping of a physical quantity. The former methods, while more practical, provide lower representativeness of the phenomenon since they do not account for the physical quantities involved in the process. In contrast, the latter methods offer greater accuracy by incorporating the underlying physics, although their implementation is more complex. Various adaptive mesh discretization methods have been proposed in the literature, including error estimators [29,30], cost functions [31–33], and machine learning approaches [34–36].

These adaptive meshing techniques generally fall into two main categories. The first, known as h-adaptivity, focuses on refining the mesh in regions with high gradients, thus increasing the number of elements. The second, less explored in the literature, is r-adaptivity, which maintains a constant number of elements but adapts their positions based on the underlying phenomena to represent, essentially redistributing the elements within the space.

While extensive efforts have been made to improve numerical simulation models using mesh refinement techniques in h-adaptivity [36–40], less attention has been given to maintaining a constant number of elements in r-adaptivity [41,42]. This aspect remains relatively underexplored, particularly regarding the effect of r-adaptivity strategies on the quality of the represented data when undergoing dimensionality reduction.

This article focuses on the reduction of deformation field representation using r-adaptivity techniques in the cold upsetting of

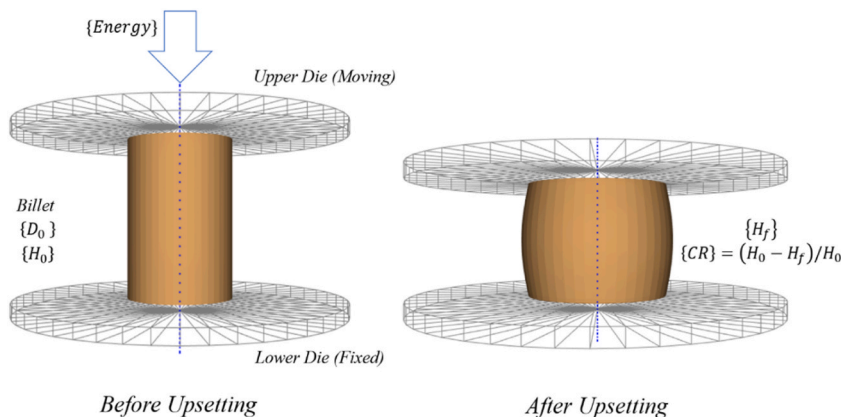


Fig. 1. Schematic of the cold cylindrical copper one-blow upsetting.

cylindrical copper billets. The study aims to evaluate the effectiveness of data reduction through Proper Orthogonal Decomposition (POD) applied to datasets derived from different discretization and r-adaptivity strategies. Four distinct approaches are examined: uniform geometry-based, gradient-based, isolines-based, and spring-energy-based meshes, each designed to optimize the quality of the reduction.

## 2. Finite element model of cylindrical upsetting

The focus of this study is on the one-blow cold upsetting process applied to cylindrical copper billets using a screw press. In this operation, the initial billet dimensions ( $D_0, H_0$ ) are subjected to compression along the billet revolution axis with a specific amount of energy ( $E$ ) until the billet achieves a final height ( $H_f$ ), as illustrated in Fig. 1. The compression ratio  $CR = (H_0 - H_f) / H_0$  of the billets ranges between 0 % and 50 %. The corresponding forging energies vary from 0 kJ to 14.45 kJ, depending on the initial dimensions of the billet and the target compression ratio.

To analyze the evolution of the deformation field for each billet, a 2D axisymmetric FE simulation was performed using FORGE® software developed by Transvalor (Fig. 2). The axisymmetric simulation represents a  $7.5^\circ$  segment of a full  $360^\circ$  revolution of the part, employing finite 3D tetrahedral elements (seen as triangles in the plane). Depending on the billet's dimensions, the number of finite elements ranged from 6000 to 12000. Mesh edge lengths averaged 0.3 mm in the billet core and were refined to 0.15 mm in external regions. The choice of element sizes was a balance between accuracy and computational efficiency, as reducing the element size by 30 % doubled the computation time. Each simulation run typically took about 15 min to complete. Remeshing is necessary during the simulation process to prevent the finite elements from becoming excessively distorted.

To capture the material behavior during forging, a reduced elastoviscoplastic Hansel-Spittel material model was employed. The flow stress was defined by Equation (1), where  $\sigma_s$  represents flow stress,  $\epsilon$  and  $\dot{\epsilon}$  denote strain and strain rate, and  $T$  stands for temperature:

$$\sigma_s = A \cdot e^{m_1 \cdot T} \cdot \epsilon^{m_2} \cdot \dot{\epsilon}^{m_3} \cdot e^{m_4 / \epsilon} \quad (1)$$

$A, m_1, m_2, m_3, m_4$  are material constants, with specific values of 411.19 MPa,  $-0.00121$ ,  $0.13$ ,  $0.01472$ , and  $0.002$  respectively. Material physical properties are listed in Table 1.

Furthermore, thermal exchanges have been assumed at  $2000 \text{ W/m}^2 \text{ K}$  between the billet and the tools, and at  $10 \text{ W/m}^2 \text{ K}$  between the air and the billet. Friction conditions follow a Coulomb limited Tresca Model:

$$\tau = \min \left( \mu \cdot \sigma_n; \bar{m} \cdot \frac{\sigma_s}{\sqrt{3}} \right) \quad (2)$$

where  $\sigma_n$  is the contact pressure;  $\mu$  and  $\bar{m}$  the friction coefficients, equal to 0.1 and 0.2, respectively. The room temperature is  $20^\circ \text{C}$ , which is also the initial temperature of the billet and the tools. The press is modeled with two rigid dies.

The deformation fields of the billets can be extracted from numerical simulations and are expressed as a 3D point cloud  $\epsilon_{FEM}$  with a variable number of points  $p$ , encompassing two spatial dimensions ( $x, y$ ) and a third dimension indicating deformation ( $\epsilon$ ), as illustrated in Fig. 2:

$$\epsilon_{FEM} = \begin{bmatrix} x_1 & y_1 & \epsilon_1 \\ x_2 & y_2 & \epsilon_2 \\ \vdots & \vdots & \vdots \\ x_p & y_p & \epsilon_p \end{bmatrix} \quad (3)$$

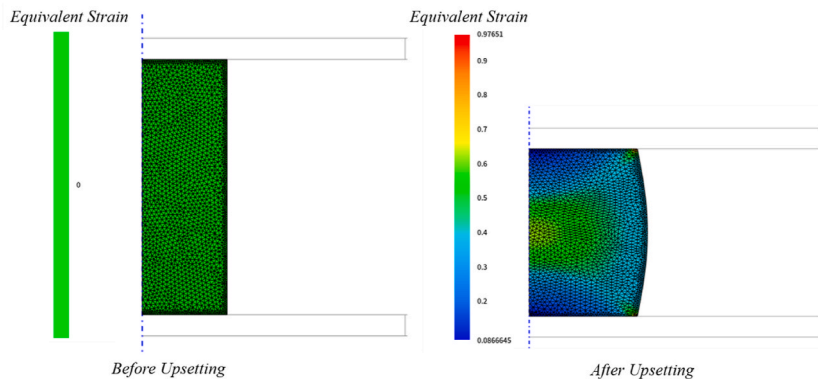


Fig. 2. Numerical 2D FE Simulation representing the deformation field of a cold copper upsetting.

**Table 1**

Physical properties of billet at 20 °C.

Material	Young's Modulus $E$ (MPa)	Poisson's ratio $\nu$	Density $\rho$ (kg/m <sup>3</sup> )	Thermal Conductivity $k$ (W/m-K)	Specific Heat $c$ (J/kg-K)
Pure Copper	110000	0.3	8100	401	435

The point cloud's coordinates correspond to the nodes of the FE simulation. To represent the deformation fields in the different upsetting cases under study, between  $p = 6000$  and  $p = 12000$  nodes are required, depending on the billet's size. This 3D point cloud poses challenges for integration into a surrogate model due to its size and variable node count. Therefore, before applying the reduced-order-model technique of POD, it is essential to employ a discretization technique. The discretization techniques utilized are detailed in the *Anisotropic meshes adaptations* section.

### 3. Generation of deformation field snapshots

The POD method, employed as a statistical approach to reduce data dimensionality, necessitates a diverse array of deformation fields representing various deformation states across different billet dimensions, consolidated into a dataset matrix (also known as a 'method of snapshots') [43]. To achieve this, a factorial design of experiments (DoE) was employed, allowing for the streamlining of the number of simulations required. Within this DoE framework, the LHS method was utilized, a well-established technique in the metal forming field, as suggested by several authors [44–46]. This method ensures an efficient exploration of the parameter space and mitigates the risk of oversampling or undersampling particular regions, thus enhancing the robustness and reliability of the results [47].

As the copper deformation is performed under cold forging conditions (where  $T/T_{solidus} < 0.3$ ), atomic thermal agitation is minimal. This results in a predominance of athermal mechanisms, such as dislocation movement, which are less dependent on time. Consequently, temporal factors are not considered, and the POD snapshots database focuses on capturing the spatial characteristics of the deformation fields rather than specific time-dependent changes.

The factors under investigation in this study are the initial diameter ( $D_0$ ) and initial height ( $H_0$ ) of the billets. The initial diameters were varied between 15 and 50 mm. For each billet, it was ensured that the compression ratio (CR) reached up to 50 %. Fifty combinations of  $[D_0, H_0]$  were created, resulting in 50 simulations. From these simulations, a total of 30000 deformation field snapshots were extracted, as each simulation provided 600 steps representing the deformation field's evolution from the billet's initial state until its final state at a compression ratio of 50 %. The deformation values span from  $\varepsilon = 0$  to  $\varepsilon = 1.5$ .

The number of nodes varies for each snapshot, making them challenging to compile into a POD-compatible matrix (see Fig. 3a). To ensure a uniform representation with a constant number of points, a discretization process is implemented. This process involves converting each deformation field into a  $k \times k$  deformation matrix  $\epsilon_d$ , with  $k = 100$ . Horizontal and vertical grids are traced within the billet's dimensions to create a regular mesh  $M_{reg} = [M_x, M_y]$  that follows its geometry:

$$M_{reg} = \begin{bmatrix} x_{1,1}, H & x_{1,2}, H & \dots & r_1, H \\ x_{2,1}, y_{2,1} & x_{2,2}, y_{2,2} & \dots & r_2, y_{2,k} \\ \vdots & \vdots & \ddots & \vdots \epsilon_{\dots, 100} \\ x_{k,1}, 0 & x_{k,2}, 0 & \dots & r_k, 0 \end{bmatrix} \quad (4)$$

where  $H$  is the billet's height,  $r_i$  is the billet radius in the  $i$ -th billet's horizontal grid, and  $x_{ij}, y_{ij}$  are the internal discretized nodal coordinates of the mesh (Fig. 3b).

The deformation values of nodal coordinates within these grids correspond to the values filling the  $k \times k$  ( $100 \times 100$ ) matrix:

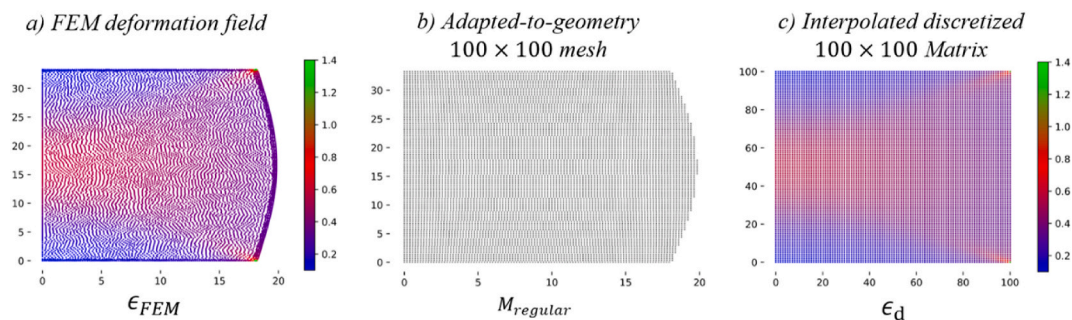


**Fig. 3.** Example of the discretization process for creating an isotropic mesh: a) Original FEM Field. b)  $100 \times 100$  adapted-to-geometry uniform mesh. c)  $100 \times 100$  Interpolated discretized matrix.

$$\epsilon_d = \begin{bmatrix} \epsilon_{1,1} & \epsilon_{1,2} & \dots & \epsilon_{1,k} \\ \epsilon_{2,1} & \epsilon_{2,2} & \dots & \epsilon_{2,k} \\ \vdots & \vdots & \ddots & \vdots \\ \epsilon_{k,1} & \epsilon_{k,2} & \dots & \epsilon_{k,k} \end{bmatrix} \quad (5)$$

Deformation values for each point in the matrix are determined using spatial interpolation, employing linear interpolation techniques (see Fig. 3c). The choice of a  $100 \times 100$  matrix size is determined through gradient analysis of subsequent fields, as explained by Ref. [23].

In this work, this isotropic mesh serves as the initial global mesh for r-adaptivity within a Proper Orthogonal Decomposition (POD) technique, allowing for the comparison of various adaptivity techniques in the following sections.

#### 4. Anisotropic meshes adaptations

An isotropic geometric-based distribution represents the simplest discretization form applied to thermomechanical fields. However, this approach overlooks the field values of local behavior, potentially leading to inadequate resolution in regions subjected to significant field variations. To address this limitation, anisotropic mesh adaptation techniques were employed.

Anisotropic mesh adaptation focuses on maintaining a constant number of elements throughout the simulation domain by locally adjusting the mesh resolution based on features such as gradients or error estimations. By moving the mesh's nodes, the resolution can be enhanced in regions experiencing high field gradients, ensuring a better capture of variations.

In this section, three distinct anisotropic mesh adaptation techniques are analyzed: mesh adaptation by gradient matrices, mesh adaptation by isolines, and mesh adaptation by a spring-energy approach. These techniques would be later compared to the initial isotropic mesh adaptation from Fig. 3.

##### 4.1. Mesh adaptation by gradient matrices

One method for r-adaptivity is to adjust the mesh based on the gradient matrices. The foundation of gradient matrix computation lies in the Sobel operator, a technique for edge detection in image processing [48]. By convolving an input matrix with the Sobel kernel, horizontal and vertical gradient matrices can be obtained. The computation of gradient matrices involves convolving  $3 \times 3$  submatrices, centered at each point of the input matrix of interest. Let  $\epsilon_d$  be the input matrix and  $G_x$  be the horizontal gradient matrix. The Sobel operator for the horizontal gradient is:

$$K_x = \begin{bmatrix} -1 & 0 & 1 \\ -2 & 0 & 2 \\ -1 & 0 & 1 \end{bmatrix} \quad (6)$$

To compute the gradient matrix  $G_x$ , a 2D convolution between the input matrix  $\epsilon_d$  and the Sobel kernel is performed:

$$c \ G_x(i,j) = \sum_{m=\max(-1,-i)}^{\min(1,k-1-i)} \sum_{n=\max(-1,-j)}^{\min(1,k-1-j)} \epsilon_d(i+m,j+n) \cdot K_x(m+1,n+1) \quad (7)$$

For the vertical gradient matrix  $G_y(i,j)$  computation, the convolution is also made, but with the Sobel operator for the vertical gradient  $K_y$ , which is the transposed matrix of the horizontal one  $K_y = K_x'$ . To quantify the overall gradient magnitude at each point in the mesh, the norm of the horizontal and vertical gradient matrices can be calculated:

$$G_{xy}(i,j) = (G_x(i,j)^2 + G_y(i,j)^2)^{1/2} \quad (8)$$

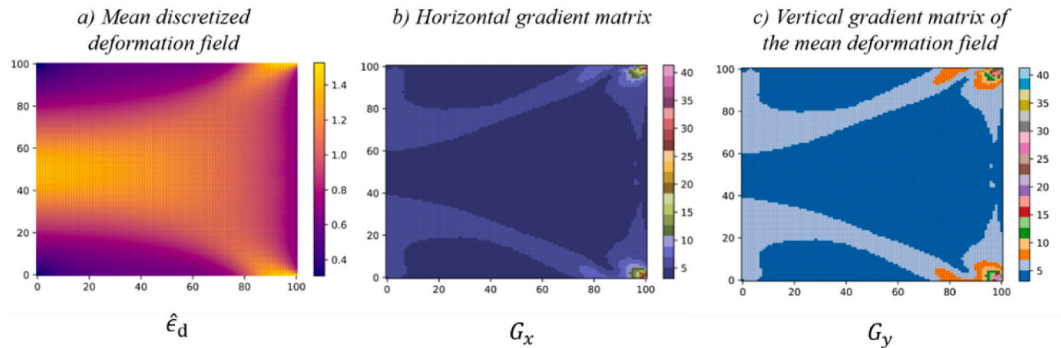


**Fig. 4.** Gradient matrix analysis for the mean deformation discretized field: a) Mean discretized field. b) Horizontal gradient matrix. c) Vertical gradient matrix.



To maintain a constant representation of the gradient matrices for any deformation field state, they are calculated after standardizing the deformation field into  $k \times k$  matrix. This ensures that both gradient matrices maintain the same  $k \times k$  size (see Fig. 4).

The r-adaptivity of the mesh from Fig. 3b following the gradient matrix results is presented as follows. Let  $CG_x(j)$  be the  $k$ -size vector containing the cumulative sum of the absolute horizontal gradients along each column  $j$ , and  $CG_y$  be the  $k$ -size vector containing the cumulative sum of the absolute vertical gradients along each row  $i$ , such as:

$$\begin{cases} CG_x(j) = \sum_{m=1}^i |G_x(m,j)| \\ CG_y(i) = \sum_{n=1}^j |G_y(i,n)| \end{cases} \quad (9)$$

Given that the cumulative sum values for the matrix  $CG_x$  and  $CG_y$  depend respectively on the gradient matrix  $G_x$  and  $G_y$  values, their sums may vary for different vectors. Therefore, a normalization of the cumulative matrix  $CG_x, CG_y$  should be done to enable the performance of r-adaptivity on the discretized isotropic mesh  $\in_d$ . This normalization ensures that the cumulative sum of each vector  $CG_x(j)$  and  $CG_y(i)$  equals 100 % in the last positions  $i = k$  and  $j = k$ , such as:

$$\begin{cases} \overline{CG}_x(j) = \frac{CG_x(j)}{\sum_{m=1}^{k=100} |G_x(m,j)|} [\%] \\ \overline{CG}_y(i) = \frac{CG_y(i)}{\sum_{n=1}^{k=100} |G_y(i,n)|} [\%] \end{cases} \quad (10)$$

To prevent incorrect values from tending towards infinity when the gradient matrix values  $G_x, G_y$  approach zero, an offset  $\omega$  is applied to the formulation:

$$\begin{cases} \overline{CG}'_x(j) = \frac{CG_x(j)}{\omega + \sum_{m=1}^{k=100} |G_x(m,j)|} [\%] \\ \overline{CG}'_y(i) = \frac{CG_y(i)}{\omega + \sum_{n=1}^{k=100} |G_y(i,n)|} [\%] \end{cases} \quad (11)$$

From this, the anisotropic gradient mesh adaptation  $GM = GM_x, GM_y$  can be computed as:

$$GM = \begin{cases} GM_x = \sum_{m=1}^k \sum_{n=1}^k r_m \cdot \overline{CG}'_x(m,n) \\ GM_y = \sum_{m=1}^k \sum_{n=1}^k H \cdot \overline{CG}'_y(n,m) \end{cases} \quad (12)$$

Fig. 5 shows the results of this anisotropic mesh adaptation for different  $\omega$  values. The choice of the ideal  $\omega = 0.02$  hinges on two factors: first, an evaluation of the adaptive mesh against the original mesh, considering both mean and standard deviation; and second, the outcomes of the reduction achieved through the POD method described in the 4th section.

The anisotropic mesh adaptation computation time for this method is 19.57 s on average. Fine-tuning the offset allows for an optimal configuration. However, the mesh structure indicates a lack of regularity, especially in the upper right and lower parts. This

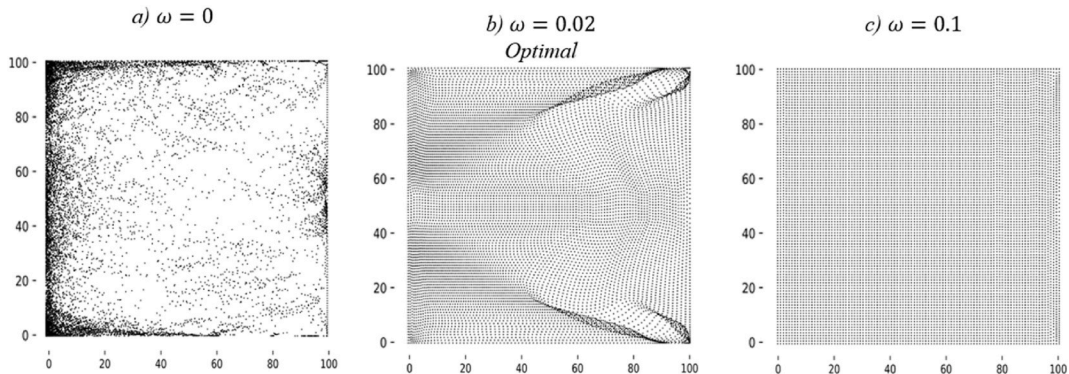


Fig. 5. Comparison of different  $\omega$  values for the gradient adaptive mesh approach: a)  $\omega = 0$ . b)  $\omega = 0.02$  (optimal). c)  $\omega = 0.1$ .

could be attributed to the normalization performed in equation (10), as it is done line by line and column by column, without considering the gradient values relative to the global values of each node. As a result, the mesh may exhibit irregularities and inconsistencies in node distribution.

#### 4.2. Mesh adaptation by isolines

A second approach, known as mesh adaptation by isolines, focuses on redistributing mesh nodes along isolines, which are curves connecting points of similar field values [49,50]. The concept relies on determining whether a point exhibits a local strain  $\varepsilon$  within a specified interval  $[\varepsilon_1, \varepsilon_2]$ , a query revisited through:

$$(\varepsilon - \varepsilon_1) \cdot (\varepsilon - \varepsilon_2) < 0 \quad (13)$$

The number of points of this kind of mesh adaptation  $IM = IM_x, IM_y$  is determined by the number of intervals  $n_i$  to consider such as  $[\varepsilon_1, \varepsilon_2, \dots, \varepsilon_{n_i+1}]$ , as well as the initial FE mesh's number of points to keep per interval.

Mesh adaptation by isolines differs from other methods in that it performs an anisotropic mesh adaptation without explicitly incorporating r-adaptivity. However, to facilitate comparison with other methods, the number of points representing this mesh method was kept nearly the same as in the initial isotropic mesh  $M_{regular}$ , being  $np_m = k \times k$ , with  $k = 100$ , resulting in 10000 points.

To achieve this, the number of points represented by the isoline mesh adaptation  $np_m$  method should indeed be calculated as the product of the number of intervals  $n_i$  and the number of points per interval  $n_{p/i}$  such as:

$$np_m = n_i \cdot n_{p/i} \quad (14)$$

An iterative algorithm is implemented in Python to determine the optimal isolines mesh adaptation. This algorithm iterates over a range of values for the number of intervals  $n_i$  and the number of points per interval  $n_{p/i}$ , respectively varying from 40 to 400 and from 25 to 250 (Fig. 6). The selection of the optimal combination is based on two criteria: a) a comparison of the isoline mesh adaptation with the original mesh properties, such as mean and standard deviation, and b) the results of the reduction using the POD method outlined in the 4th section. The selected mesh  $IM$  is composed of 400 isolines, with 25 points per isoline, resulting in a total of 10000 points.

The anisotropic mesh adaptation computation time for this mesh is 4.13 s on average. The mesh obtained using the isoline method follows a pattern similar to the average deformation field and the gradient matrix-based mesh. However, by taking discrete gradient values to create isolines, irregularities and areas with significantly reduced node concentration are created, specially in the middle region of the part. While this type of mesh can be optimal if the number of isolines is increased considerably, this would result in higher computational cost and larger data size compared to other methods.

#### 4.3. Mesh adaptation by a spring-energy approach

The spring-energy approach is one technique that aims to visualize the original isotropic mesh as a 2D spring network, where each position of the mesh  $M_{regular}(i, j)$  is seen as a node of the spring network. The initial spring regular mesh is not supposed to be in equilibrium, as its based on the billet's geometry and not on the deformation field variations. To reflect this, a distinct stored energy is assigned to each spring. This energy is determined by the horizontal and vertical gradients of equation (7) respectively for vertical and horizontal springs. The stored energy of a spring can be defined as:

$$E = k \cdot (l - l_0)^2 / 2 \quad (15)$$

where  $k$  represents the constant spring stiffness,  $l$  denotes the actual spring length, and  $l_0$  stands for the initial spring length. Assuming the initial spring length  $l_0$  negligible compared to  $l$  (i.e.,  $l \gg l_0$ ), thus equation (15) can be expressed as follows:

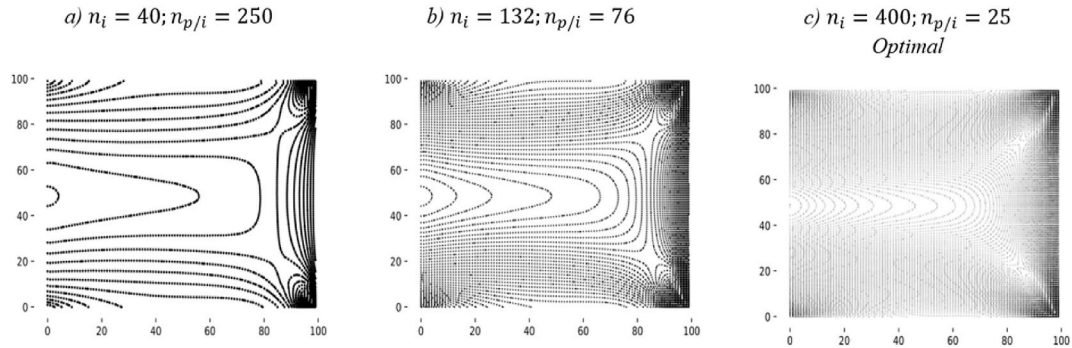


**Fig. 6.** Optimal testing of isoline mesh adaptation with different number of isolines and points per isoline: a)  $n_i = 40; n_{p/i} = 250$ . b)  $n_i = 132; n_{p/i} = 76$ . c)  $n_i = 400; n_{p/i} = 25$ .



$$E \cong k \cdot l^2 / 2 \quad (16)$$

Hence, the spring energy before  $E_b$  and after  $E_a$  the anisotropic mesh r-adaptivity, and consequently, each spring length in the adapted mesh could be related as follows:

$$l_a = (E_a/E_b)^{1/2} \cdot l_b \quad (17)$$

where  $l_b = 1$  as it is the length of a spring that comes from the  $100 \times 100$  standardize isotropic mesh and  $l_a$  is anisotropic mesh length. Now, considering that the original mesh is a regular grid with horizontal and vertical lines within a  $k \times k$  matrix, it follows that the sum of the spring lengths along any particular row  $i$  or column  $j$  should be equal to  $k$  (see Fig. 7). This implies that the nodes of the springs at the borders of the  $100 \times 100$  matrix do not move.

This condition is fulfilled if the mesh adaptation is performed separately in each direction (vertical and horizontal), such as:

$$\sum_{m=1}^k l_{a,m} = \sum_{m=1}^k l_{b,m} = k \quad (18)$$

where  $m$  could be a specific row  $i$  or column  $j$  of the original mesh matrix  $k \times k$ . And then, combining equations (17) and (18), one could readily deduce that:

$$k = \sum_{m=1}^k (E_a/E_b)^{1/2} \quad (19)$$

The principle of this method is to distribute energy among all springs by adjusting the length  $l_{a,m}$ , thereby balancing the energies and maintaining  $E_a$  constant for all springs. From this, the following formulation can be derived:

$$E_a = \left( \frac{k}{\sum_{m=1}^k \frac{1}{E_b^{1/2}}} \right)^2 \quad (20)$$

Thus, each final spring length can be expressed as:

$$l_a = \frac{E_b^{1/2} \cdot k}{\sum_{m=1}^k \frac{1}{E_b^{1/2}}} \cdot l_b \quad (21)$$

An offset is applied to this last formulation to prevent incorrect values from tending towards infinity when the gradient matrix and the energy values, are approaching zero:

$$l_a^2 = \frac{(E_b + \varphi)^{1/2} \cdot k}{\sum_{m=1}^k \frac{1}{(E_b + \varphi)^{1/2}}} \cdot l_b \quad (22)$$

where  $\varphi$  is the offset value,  $E_b$  comes from the horizontal and vertical gradient matrices, and  $l_b$  comes from the isotropic mesh positions  $M_{regular}$ . Iteratively evaluating this equation for the rows and columns of the initial isotropic mesh provides the corrected positions of the mesh nodes, and thus, the anisotropic adapted mesh  $M_{energy}$ . Fig. 8 shows the results of this anisotropic mesh adaptation for different  $\varphi$  values. The selection of the optimal  $\varphi = 0.01$  is based on two criteria: a) a comparison of the adaptative mesh with the original mesh, regarding the mean and standard deviation, and b) the results of the reduction using the POD method outlined in the 4th

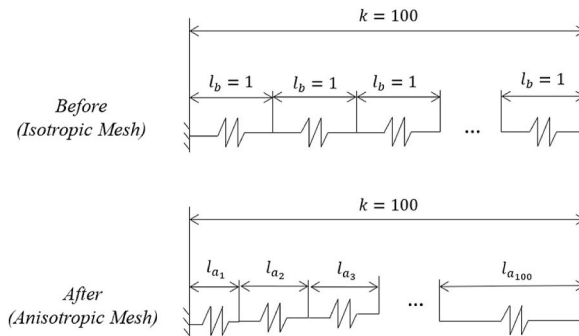


Fig. 7. Anisotropic mesh r-adaptivity using spring-energy-based method in one direction.

section.

The anisotropic mesh adaptation computation time for this method is 10.86 s on average. At a glance, the optimal mesh from this method exhibits greater smoothness and regularity among the nodes compared to other methods. This is due to the use of a spring network with well-defined boundary conditions. This approach ensures a more uniform and continuous adaptation, reducing irregularities and improving the overall quality of the mesh.

## 5. POD reduced-order modeling for different mesh-adapted deformation fields

The isotropic mesh as well as the gradient-based, isoline-based, and spring-energy-based adaptive meshes are employed to interpolate the 30000 FE deformation fields from the initial database. The vectorization of each deformation field yields a 10000-size vector, resulting in four discretized databases, sized  $30000 \times 10000$  each. Reduction using the POD method is applied to each database, laying the groundwork for surrogate model development [43,51]. The objective is to represent any deformation field using identical vector modes, allowing variations solely in the vector coefficients. Additionally, all databases undergo centering and scaling using the mean deformation field and mean standard deviation to enhance results.

A consistent selection of three representative modes has been made for all the POD reductions to facilitate the comparison of reduction results across different meshes, leading to a deformation field approximation:

$$\epsilon_d \cong \hat{\epsilon}_d + \sigma_\epsilon \sum_{i=1}^{m=3} b_i \cdot \varphi_i \quad (23)$$

where  $\hat{\epsilon}_d$  and  $\sigma_\epsilon$  are the mean deformation field and the standard deviation, respectively;  $\varphi_i$  is the  $i_{th}$  basis function or mode obtained from the POD; and,  $b_i$  is the coefficient associated with the  $i_{th}$  mode.

## 6. Results and discussion

The database comprising 30000 deformation field snapshots serves as the basis for gradient analysis. However, rather than computing horizontal and vertical gradient matrices for all the snapshots, the focus is narrowed down to study the vertical and horizontal gradient matrix for the mean isotropic deformation field  $\hat{\epsilon}_d$ , which is of  $100 \times 100$  size.

The resulting discretized meshes, along with the geometric adaptation of these meshes for a specific billet are presented for each method in Fig. 9. Despite the variations in discretization approaches, the three anisotropic meshes consistently exhibit a similar deformation behavior, forming an "x-type" geometry within the forged part. This geometric pattern is attributed to the material flow of the upsetting operations and is observed not only in deformation fields (as shown in Fig. 4a) but also in other fields such as temperature fields [52]. However, depending on the discretization method employed, the distribution of nodes across this "x-type" geometry may vary, resulting in different meshes.

Comparing the different mesh adaptation methods, the isoline method demonstrates the quickest adaptation time at 4.13 s. Despite its speed, it can produce irregularities and areas with reduced node concentration, particularly in the middle regions of the mesh. While increasing the number of isolines could enhance accuracy, it would also lead to increased computational costs and larger data sizes. The energy-based method, taking 10.86 s for adaptation, provides a good balance between speed and quality. It offers a smoother and more regular mesh, attributed to the well-defined boundary conditions of the spring network, resulting in a more uniform node distribution compared to the gradient matrix-based and isoline methods. In contrast, the gradient matrix-based method, with an adaptation time of 19.57 s, is the slowest method. This method can exhibit irregularities in node distribution due to local normalization practices. Overall, all three methods are relatively fast compared to the time-consuming process of interpolating the deformation field into the adaptive meshes, which takes between 2 and 4 h for each database of 30,000 deformation field snapshots (similar for isotropic mesh interpolation).

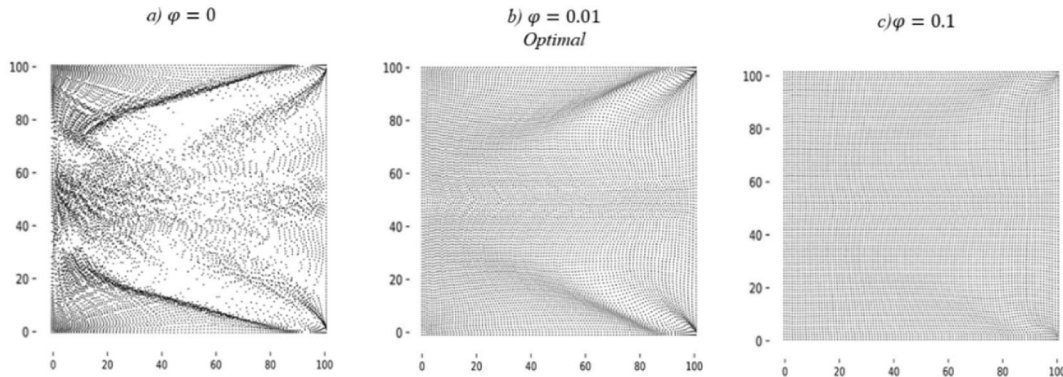
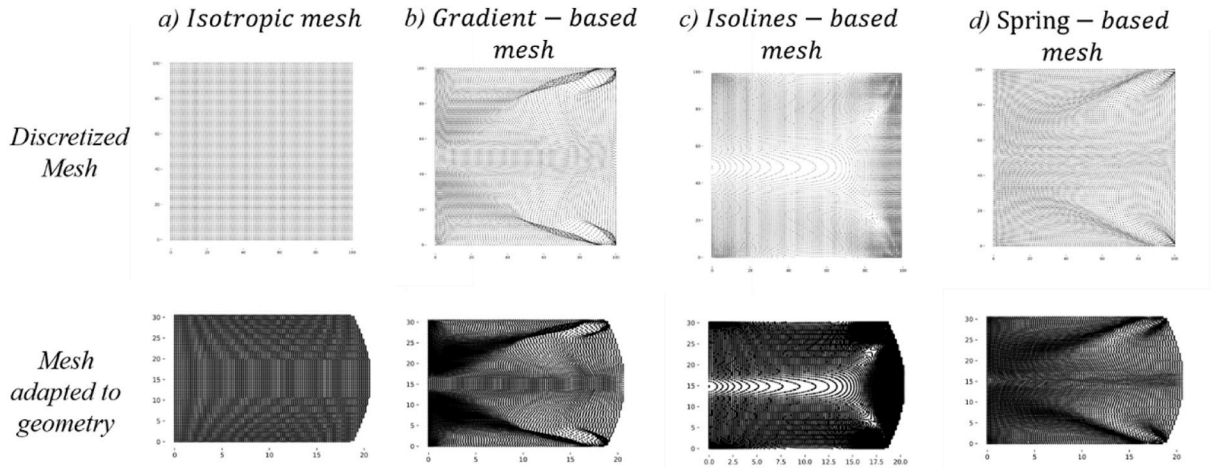


Fig. 8. Comparison of different  $\varphi$  values for the spring-energy adaptive mesh approach: a)  $\varphi = 0$ , b)  $\varphi = 0.01$  (optimal), c)  $\varphi = 0.1$ .



**Fig. 9.** Discretized square meshes and discretized meshes adapted to geometry for: a) Isotropic mesh b) Gradient-based mesh c) Isolines-based mesh d) Spring-energy-based mesh.

The calculations for these mesh adaptation methods were performed on a machine equipped with a 12th Gen Intel® Core™ i7-12800H processor running at 2.40 GHz and 8 GB of RAM. The memory usage during all anisotropic mesh adaptivity methods remained below 2 GB, ensuring moderate impact on system performance.

Fig. 10 presents the Kernel Density Estimator (KDE), a statistical tool used to estimate the probability density function, illustrating in this case the distribution of nodes across the 100x100 space. The isotropic mesh exhibits a uniform density that does not correspond to the deformation field under study. The isolines method results in a concentration of points in certain areas of the field while leaving other regions sparse, thus not fully representing the mean deformation field. In contrast, both the gradient-based and spring-based meshes capture the deformation field more accurately. Among these, the spring-based mesh provides a higher level of fidelity, with a clear "x-type" distribution of the upsetting process visible across the domain.

In order to compare the four types of mesh, the cumulative energy from the POD reduction is presented for the first modes for each discretized mesh in Fig. 11. Among the cases examined, the isotropic mesh demonstrates the least favorable performance, with the first mode capturing only approximately 60 % of the cumulative energy. To reach 80 % cumulative energy, approximately 70 modes are required. In contrast, the spring-energy-based approach showcases the most promising behavior, with the first mode capturing about 75 % of the cumulative energy, and over 80 % achieved with just two modes. The gradient-based and isolines-based methods necessitate four and three modes, respectively, to attain 80 % cumulative energy. Even though the data represent the same physical process, the variation in mesh type enables the capture of differing levels of local variation. This variance results in the representation of data with varying levels of fidelity.

The Mean Absolute Error (MAE) is presented as error metric for reconstructing different POD databases using three modes (Fig. 12). On the previous figure it appears that, all anisotropic meshes achieve 80 % of the cumulative energy with three modes, whereas the isotropic mesh reaches only around 67 % with the same number of modes. This discrepancy explains why the reconstruction errors are lower with anisotropic than with isotropic mesh adaptation, as anisotropic meshes retain more information during a similar reduction process. Among the methods, the spring-energy mesh-based approach maintains superior performance, with a MAE lower than 0.01.

The computation time for POD reconstruction of a deformation field using three modes remains consistently below 500 ms across all methods. This deployment time ensures that any of the mesh adaptivity methods can be effectively used in real-time applications with acceptable accuracy.

Fig. 13 displays the Mean Absolute Error (MAE) for all discretization methods with a varying number of modes, ranging from 1 to 6

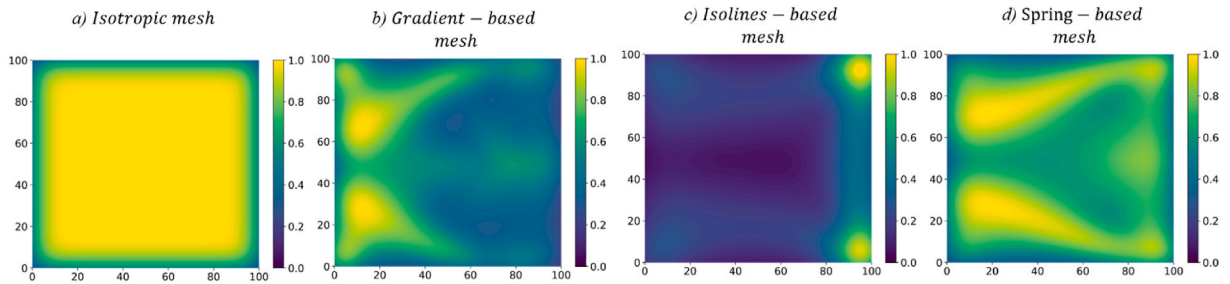


**Fig. 10.** Kernel Density Estimator (KDE) applied to node positions: a) Isotropic mesh b) Gradient-based mesh c) Isolines-based mesh d) Spring-energy-based mesh.

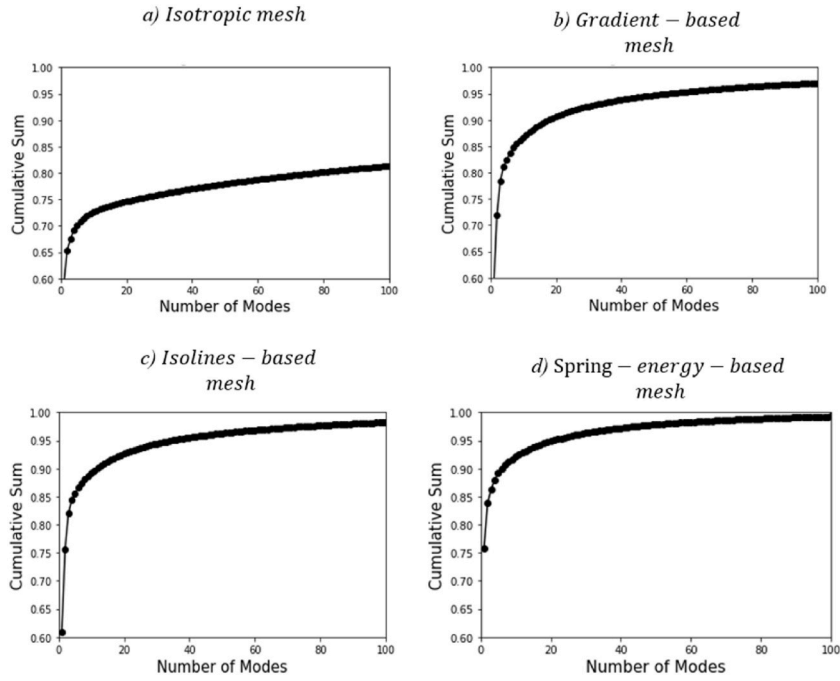


**Fig. 11.** Cumulative energy from the POD for each discretized mesh: a) Isotropic mesh b) Gradient-based mesh c) Isolines-based mesh d) Spring-energy-based mesh.

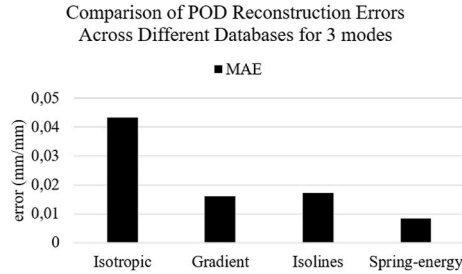


**Fig. 12.** Error metrics in POD reconstructions with 3 modes for each discretized mesh.

modes, plotted on a logarithmic scale. After the utilization of four modes, all discretized meshes exhibit diminishing errors. Nevertheless, the asymptotic values vary significantly across cases, with errors dropping below 0.005 for the spring-energy-based method and reaching approximately 0.017 for the isotropic mesh.

Among the explored techniques, the spring-energy approach proposed in this study emerged as particularly promising, showcasing superior performance in enhancing data representation quality. This can be attributed to its adept fit to gradients present in the data, as well as to the connectivity along the springs, which contributes to the smoothness of the mesh. Consequently, the mesh generated through the spring-energy-based method is better equipped to capture subtle nuances in thermomechanical fields, thereby reducing interpolation errors when reconstructing from a limited number of POD modes.

More generally by testing various mesh adaptation strategies coupled with Proper Orthogonal Decomposition (POD) several insights have emerged regarding mesh adaptation, along with other implications for data reduction quality.

- **Matrix Size Consideration:** The choice of a square  $100 \times 100$  matrix as the initial discretized matrix was made for practical reasons, aiming to balance data representation and computational efficiency. Although the influence of matrix size on result quality was not explicitly addressed in our study, it remains an important consideration for future research to explore the effects of varying matrix sizes on the accuracy and efficiency of data representations.
- **Generalizability of Adaptivity Techniques:** Unlike r-adaptivity techniques based on domain-specific objective functions, the use of non-domain-specific mesh adaptivity techniques allows for greater generalization. In fact, the three anisotropic methods presented in this work are versatile and can be applied across various thermomechanical fields, such as temperature fields, stress fields, and

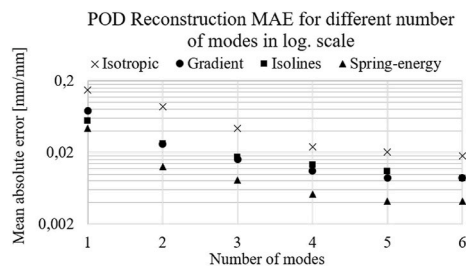


Fig. 13. Mean Absolute Error in POD reconstructions for different discretized meshes in a logarithmic scale.

beyond, as the gradient matrix can be calculated in all these cases, further extending the applicability of these methods beyond just deformation field analysis.

- **Gradient Matrix Utilization:** The study revealed the effectiveness of incorporating gradient matrices as a valuable approach for adapting meshes across different discretization techniques. By analyzing horizontal and vertical gradients, mesh resolution could be adjusted based on field variations. However, it became evident that applying an offset was crucial in regions where gradient values were approaching zero, ensuring the stability and accuracy of mesh adaptation, particularly in areas with minimal gradient variations.
- **Offset setting:** Applying an offset is crucial in regions where gradient values approach zero. This ensures the stability and accuracy of mesh adaptation, especially in areas with minimal gradient variations. However, tuning the offset remains dependent on the specific case and the thermomechanical field under study.

## 7. Conclusions

This study investigated and compared various discretization and mesh adaptivity strategies for enhancing data representation fidelity in forging processes using POD. The findings underscored the importance of the mesh adaptation technique to achieve accurate and efficient data representations for surrogate modeling. Anisotropic mesh adaptations, including gradient-based, isolines-based, and spring-energy-based approaches, exhibited superior performance in capturing local field variations compared to the isotropic mesh. These techniques facilitated better representations of deformation fields with the same amount of data. Additionally, this study highlights that the utilization of the gradient matrix is particularly beneficial for mesh adaptation, significantly contributing to enhanced data representation quality. The results indicate that the spring-energy-based method emerged as the most promising, showcasing a smoother mesh and accurately capturing intricate deformation patterns.

In conclusion, this research contributes to advancing the understanding of how different mesh r-adaptivity approaches can enhance the efficiency and accuracy of data representation in industrial processes. Future studies should explore the implementation of these mesh adaptation techniques in data-driven modeling and analysis, focusing on their impact on model accuracy and effectiveness.

## Funding

This study was funded by the Technical Center for Mechanical Industry (CETIM) and the Carnot Institut ARTS (Research Actions for Technology and Society)

## CRediT authorship contribution statement

**David Uribe:** Writing – review & editing, Writing – original draft, Software, Investigation, Data curation. **Camille Durand:** Writing – review & editing, Validation, Conceptualization. **Cyrille Baudouin:** Writing – review & editing, Methodology, Formal analysis. **Régis Bigot:** Supervision, Resources, Funding acquisition.

## Declaration of competing interest

The authors declare that they have no known competing financial interests or personal relationships that could have appeared to influence the work reported in this paper.

## Acknowledgment

We would like to sincerely thank the Technical Center for Mechanical Industry (CETIM) for their financial support in this research project. We would also like to thank Daniel Boehm and Alexandre Fendler for their technical support during the various tests conducted.



## Data availability

No data was used for the research described in the article.

## References

- [1] Jasleen Kaur, B.S. Pabla, S.S. Dhami, et al.Chandigarh Nitttr, A review on field areas of research in forging process using FEA, IJERT V5 (1) (2016) IJERTV5IS010310, <https://doi.org/10.17577/IJERTV5IS010310> janv.
- [2] V.T. Dang, C. Labergere, et al.P. Lafon, POD surrogate models using adaptive sampling space parameters for springback optimization in sheet metal forming, Procedia Eng. 207 (2017) 1588–1593, <https://doi.org/10.1016/j.proeng.2017.10.1053>, janv.
- [3] M. Hamdaoui, G. Le Quilliec, P. Breikopf, et al.P. Villon, POD surrogates for real-time multi-parametric sheet metal forming problems, Int J Mater Form 7 (3) (sept. 2014) 337–358, <https://doi.org/10.1007/s12289-013-1132-0>.
- [4] M. Ryser, F.M. Neuhauser, C. Hein, P. Hora, et al.M. Bambach, Surrogate model-based inverse parameter estimation in deep drawing using automatic knowledge acquisition, Int. J. Adv. Manuf. Technol. 117 (3–4) (2021) 997–1013, <https://doi.org/10.1007/s00170-021-07642-x>, nov.
- [5] K. Slimani, M. Zaaif, et al.T. Balan, « Accurate surrogate models for the flat rolling process, Int. J. Material Form. 16 (2023), <https://doi.org/10.1007/s12289-023-01744-5> mars.
- [6] R.K. Tan, C. Qian, M. Wang, et al.W. Ye, An efficient data generation method for ANN-based surrogate models, Struct Multidisc Optim 65 (3) (févr. 2022) 90, <https://doi.org/10.1007/s00158-022-03180-6>.
- [7] F. Teng, G. Menary, S. Malinov, S. Yan, et al.J.B. Stevens, Predicting the multiaxial stress-strain behavior of polyethylene terephthalate (PET) at different strain rates and temperatures above T<sub>g</sub> by using an Artificial Neural Network, Mech. Mater. 165 (2022) 104175, <https://doi.org/10.1016/j.mechmat.2021.104175> févr.
- [8] B. de Gooijer, J. Havinga, H. Geijselaers, et al.T. Van den Boogaard, Evaluation of POD based surrogate models of fields resulting from nonlinear FEM simulations, Advanced Modeling and Simulation in Engineering Sciences 8 (2021), <https://doi.org/10.1186/s40323-021-00210-8> déc.
- [9] F. Chinesta, P. Ladeveze, et al.E. Cueto, A short review on model order reduction based on proper generalized decomposition, Arch. Comput. Methods Eng. 18 (4) (2011) 395–404, <https://doi.org/10.1007/s11831-011-9064-7>, nov.
- [10] E. Cueto, F. Chinesta, et al.Huerta, Model order reduction based on proper orthogonal decomposition, in: F. Chinesta, et al.P. Ladeveze (Eds.), Separated Representations and PGD-Based Model Reduction: Fundamentals and Applications, Springer, Vienna, 2014, pp. 1–26, [https://doi.org/10.1007/978-3-7091-1794-1\\_1](https://doi.org/10.1007/978-3-7091-1794-1_1).
- [11] P. Benner, S. Grivet-Talocia, A. Quarteroni, G. Rozza, W. Schilders, et al.L.M. Silveira, Éd, System- and Data-Driven Methods and Algorithms, vol. 1, De Gruyter, 2021, <https://doi.org/10.1515/9783110498967>.
- [12] Z.K. Hardy, et al.J.E. Morel, Proper orthogonal decomposition mode coefficient interpolation: a non-intrusive reduced-order model for parametric reactor kinetics, Nucl. Sci. Eng. 198 (4) (2024) 832–852, <https://doi.org/10.1080/00295639.2023.2218581>, avr.
- [13] B. de Gooijer, J. Hazrati, H. Geijselaers, et al.T. Van den Boogaard, On the Choice of Basis in Proper Orthogonal Decomposition-Based Surrogate Models, vol. 2113, 2019, <https://doi.org/10.1063/1.5112635>.
- [14] M. Ouhelou, et al.C. Allery, A fast and robust sub-optimal control approach using reduced order model adaptation techniques, Appl. Math. Comput. 333 (2018) 416–434, <https://doi.org/10.1016/j.amc.2018.03.091>, sept.
- [15] T. Li, T. Pan, X. Zhou, K. Zhang, et al.J. Yao, Non-intrusive reduced-order modeling based on parametrized proper orthogonal decomposition, Energies 17 (1) (2024), <https://doi.org/10.3390/en17010146>. Art. no 1, janv.
- [16] M.B. Russo, P. Franciosa, A. Greco, et al.S. Gerbino, Reduced-order modelling for real-time physics-based variation simulation enhanced with adaptive sampling and optimized interpolation, Int. J. Adv. Manuf. Technol. 132 (7) (2024) 3709–3734, <https://doi.org/10.1007/s00170-024-13493-z>, juin.
- [17] M.-L. Giorgi, H. Duval, et al.M. Balabane, The proper orthogonal decomposition: a powerful tool for studying drop oscillations, Rev. Sci. Instrum. 92 (11) (nov. 2021) 113903, <https://doi.org/10.1063/5.0056004>.
- [18] G.T. Havinga, Optimization and control of metal forming processes (2016), <https://doi.org/10.3990/1.9789036541480> juin.
- [19] A. Radermacher, S. Reese, et al.A.M.H. Hadoush, « Selective proper orthogonal decomposition model reduction for forming simulations, Proc. Appl. Math. Mech. 13 (1) (2013) 115–116, <https://doi.org/10.1002/pamm.201310053>.
- [20] D. Kloeser, J. Martschin, T. Meurer, et al.E. Tekkaya, Reduced order modelling for spatial-temporal temperature and property estimation in a multi-stage hot sheet metal forming process, Advances in Industrial and Manufacturing Engineering 3 (nov. 2021) 100055, <https://doi.org/10.1016/j.aime.2021.100055>.
- [21] C. Ghatnats, Optimization of composite forming processes using nonlinear thermal models and the proper generalized decomposition, in: 2016 3rd International Conference On Advances In Computational Tools For Engineering Applications (ACTEA), 2016, pp. 131–136, <https://doi.org/10.1109/ACTEA.2016.7560126>. Zouk Mosbeh, Lebanon, juill.
- [22] D. Uribe, C. Baudouin, C. Durand, et al.R. Bigot, Predictive control for a single-blow cold upsetting using surrogate modeling for a digital twin, Int J Mater Form 17 (1) (déc. 2023) 7, <https://doi.org/10.1007/s12289-023-01803-x>.
- [23] A. Midouai, C. Baudouin, D. Florence, et B. Régis, Surrogate model to describe temperature field in real-time for hot forging (2024), <https://doi.org/10.21741/9781644903131-95>.
- [24] Q. Wang, et al., Acceleration of Inverse Design Process on Adaptive Mesh, Optics Express, 2021. Consulté le: 30 août 2024. [En ligne]. Disponible sur: <https://www.semanticscholar.org/paper/Acceleration-of-inverse-design-process-on-adaptive-Wang-Liu/4d92f5908377dd40023d3a0941d9ebd5a014dfe6>.
- [25] C. Gräßle, et al.M. Hinze, POD reduced-order modeling for evolution equations utilizing arbitrary finite element discretizations, Adv. Comput. Math. 44 (6) (2018) 1941–1978, <https://doi.org/10.1007/s10444-018-9620-x>, déc.
- [26] T. Falk, C. Schwarz, et al.W.G. Drossel, Realtime prediction of self-pierce riveting joints - prognosis and visualization based on simulation and machine learning, KEM 926 (2022) 1479–1488, <https://doi.org/10.4028/p-5fjp40>, juill.
- [27] S. Chaturantabut, D.C. Sorensen, Nonlinear Model Reduction via Discrete Empirical Interpolation, in: SIAM Journal on Scientific Computing 32, Society for Industrial & Applied Mathematics (SIAM), Jan. 2010, pp. 2737–2764, <https://doi.org/10.1137/090766498>.
- [28] P.E. Farrell, M.D. Piggott, C.C. Pain, G.J. Gorman, C.R. Wilson, Conservative interpolation between unstructured meshes via supermesh construction. Computer Methods in Applied Mechanics and Engineering 198, Elsevier BV, 2009, pp. 2632–2642. <https://doi.org/10.1016/j.cma.2009.03.004>. Issues 33–36.
- [29] C. Labergere, A. Rassinoux, et al.K. Saanouni, Improving numerical simulation of metal forming processes using adaptive remeshing technique, Int. J. Material Form. 1 (2008) 539–542, <https://doi.org/10.1007/s12289-008-0255-1>, avr.
- [30] A. Bergam, A. Chakib, A. Nachaoui, et al.M. Nachaoui, Adaptive mesh techniques based on a posteriori error estimates for an inverse Cauchy problem, Appl. Math. Comput. 346 (2019) 865–878, <https://doi.org/10.1016/j.amc.2018.09.069>, avr.
- [31] R. Abdoola, G. Noel, B. Van Wyk, et al.E. Monacelli, Correction of Atmospheric Turbulence Degraded Sequences Using Grid Smoothing, vol. 6754, 2011, p. 327, [https://doi.org/10.1007/978-3-642-21596-4\\_32](https://doi.org/10.1007/978-3-642-21596-4_32).
- [32] E. Monacelli, R. Abdoola, G. Noel, et al.B. Van Wyk, Rishaad Abdoola, Guillaume Noel, Barend J. van Wyk, Eric Monacelli, Correction of Atmospheric Turbulence Degraded Sequences Using Grid Smoothing, vol. 2, ICIAR, 2011, pp. 317–327, 2011.
- [33] G. Noel, K. Djouani, et al.Y. Hamam, Grid smoothing: a graph-based approach, in: I. Bloch, et al.R.M. Cesar (Eds.), Progress in Pattern Recognition, Image Analysis, Computer Vision, and Applications, vol. 6419, Springer Berlin Heidelberg, Berlin, Heidelberg, 2010, pp. 153–160, [https://doi.org/10.1007/978-3-642-16687-7\\_24](https://doi.org/10.1007/978-3-642-16687-7_24).
- [34] J. Yang, et al., Multi-agent reinforcement learning for adaptive mesh refinement, Adaptive Agents and Multi-Agent Systems (2022), <https://doi.org/10.48550/arXiv.2211.00801>.

- [35] J. Phommachanh, Mesh adaptation using machine learning, M.S., Ann Arbor, United States Consulté le: 17 novembre 2023. [En ligne]. Disponible sur, <https://www.proquest.com/docview/2640413312/abstract/B7B21868A9894AE4PQ/1>, 2021.
- [36] K.J. Fidkowski, et al.G. Chen, Metric-based, goal-oriented mesh adaptation using machine learning, J. Comput. Phys. 426 (2021) 109957, <https://doi.org/10.1016/j.jcp.2020.109957> févr.
- [37] A. Loseille, Unstructured mesh generation and adaptation, in: Handbook of Numerical Analysis, vol. 18, Elsevier, 2017, pp. 263–302, <https://doi.org/10.1016/bs.hna.2016.10.004>.
- [38] C.J. Vogl, I. Joseph, et al.M. Holec, Mesh refinement for anisotropic diffusion in magnetized plasmas, Comput. Math. Appl. 145 (sept. 2023) 159–174, <https://doi.org/10.1016/j.camwa.2023.06.019>.
- [39] S. Wittschieber, A. Rangarajan, G. May, et M. Behr, Metric-based anisotropic mesh adaptation for viscoelastic flows, Comput. Math. Appl. 151 (2023) 67–79, <https://doi.org/10.1016/j.camwa.2023.09.031>, déc.
- [40] R. Hartmann, et al., Space adaptive methods/meshing, in: C. Hirsch, K. Hillewaert, R. Hartmann, V. Couaillier, J.-F. Boussuge, F. Chalot, S. Bosniakov, et al. W. Haase (Eds.), TILDA: towards Industrial LES/DNS in Aeronautics: Paving the Way for Future Accurate CFD - Results of the H2020 Research Project TILDA, Funded by the European Union, 2015–2018, Springer International Publishing, Cham, 2021, pp. 103–190, [https://doi.org/10.1007/978-3-030-62048-6\\_4](https://doi.org/10.1007/978-3-030-62048-6_4).
- [41] A. Nagarajan, et al.S. Soghrati, Conforming to interface structured adaptive mesh refinement: 3D algorithm and implementation, Comput. Mech. 62 (5) (2018) 1213–1238, <https://doi.org/10.1007/s00466-018-1560-2>, nov.
- [42] M. Cho, et al.S. Jun, « r-Adaptive mesh generation for shell finite element analysis, J. Comput. Phys. 199 (1) (sept. 2004) 291–316, <https://doi.org/10.1016/j.jcp.2004.02.007>.
- [43] H. Mohamed, G. Le Quilliec, P. Breitenkopf, et al.P. Villon, Surrogate POD models for parametrized sheet metal forming applications, KEM 554–557 (2013) 919–927. <https://dx.doi.org/10.4028/www.scientific.net/KEM.554-557.919>, juin.
- [44] F. Zhu, Z. Wang, et al.M. Lv, Multi-objective optimization method of precision forging process parameters to control the forming quality, Int. J. Adv. Manuf. Technol. 83 (9) (2016) 1763–1771, <https://doi.org/10.1007/s00170-015-7682-1>, avr.
- [45] J.H. Wiebenga, M. Weiss, B. Rolfe, et al.A.H. van den Boogaard, Product defect compensation by robust optimization of a cold roll forming process, J. Mater. Process. Technol. 213 (6) (2013) 978–986, <https://doi.org/10.1016/j.jmatprotec.2013.01.006>, juin.
- [46] J.H. Wiebenga, E.H. Atzema, et al.A.H. van den Boogaard, Stretching the limits of forming processes by robust optimization: a numerical and experimental demonstrator, J. Mater. Process. Technol. 217 (2015) 345–355, <https://doi.org/10.1016/j.jmatprotec.2014.11.018>, mars.
- [47] R. Alizadeh, J.K. Allen, et al.F. Mistree, Managing computational complexity using surrogate models: a critical review, Res Eng Design 31 (3) (2020) 275–298, <https://doi.org/10.1007/s00163-020-00336-7>, juill.
- [48] O. Vincent, et al.O. Folorunso, A descriptive algorithm for Sobel image edge detection, in: présenté à InSITE 2009: Informing Science + IT Education Conference, 2009, <https://doi.org/10.28945/3351>.
- [49] J. Canales, J.A. Tárrago, et al.A. Hernández, An adaptive mesh refinement procedure for shape optimal design, Adv. Eng. Software 18 (2) (1993) 131–145, [https://doi.org/10.1016/0965-9978\(94\)90007-8](https://doi.org/10.1016/0965-9978(94)90007-8), janv.
- [50] M. Piggott, P. Farrell, C. Wilson, G. Gorman, et C. Pain, Anisotropic mesh adaptivity for multi-scale ocean modelling, Philosophical transactions. Series A, Mathematical, physical, and engineering sciences 367 (2009) 4591, <https://doi.org/10.1098/rsta.2009.0155>, 611, nov.
- [51] H. Kang, Z. Tian, G. Chen, L. Li, et al.T. Wang, Application of POD reduced-order algorithm on data-driven modeling of rod bundle, Nucl. Eng. Technol. 54 (1) (2022) 36–48, <https://doi.org/10.1016/j.net.2021.07.010>, janv.
- [52] L. Yuan, Q. Wei, L. Han, D. Shan, et al.B. Guo, A new hot forging method for the die temperature higher than the billet temperature, Int. J. Adv. Des. Manuf. Technol. 116 (2021) 1–12, <https://doi.org/10.1007/s00170-021-07656-5>, oct.